ADVANCED ENERGY MATERIALS
www.advenergymat.de

Stable Cycling of Sodium All-Solid-State Batteries with High-Capacity Cathode Presodiation

*Wei Tang, Dapeng Xu, Junlin Wu, Dong Ju Lee, Alexander Fuqua, Feng Li, Yuju Jeon, Wenjuan Bian, and Zheng Chen**

Sodium all-solid-state batteries (NaSSBs) with an alloy-type anode (e.g., Sn and Sb) offer superior capacity and energy density compared to hard carbon anode. However, the irreversible loss of Na^+ at the alloy anode during the initial cycle results in diminished capacity and stability, impairing full-cell performance. This study presents an easy-to-implement cathode presodiation strategy by employing a Na-rich material to address these challenges. Leveraging the high theoretical capacity and suitable voltage window, Na_2S is chosen as the Na donor, which is activated by creating a mixed electron-ion conducting network, delivering a high capacity of 511.7 mAh g^{-1}. By adding a small amount (i.e., 3 wt.%) of Na_2S to the cathode composite, a $NaCrO_2$ || Sn full cell demonstrated capacity improvement from 90.8 to 118.2 mAh g^{-1} (based on cathode mass). The capacity-balanced full cell can thus cycle to more than 300 times with >90% capacity retention. This work provides a practical solution to enhance the full-cell performance and advance the transformation from half-cell to full-cell applications of NaSSBs.

1. Introduction

With the widespread adoption of electronic devices and the increasing use of renewable energies, interest in energy storage devices like batteries has surged. Despite the market dominance, lithium-ion batteries (LIBs) face limitations due to resource availability and sustainability concerns. As an alternative, sodium-ion batteries (SIBs) have gained attention due to earth-abundant sodium (Na) and cost-effective transition metal-based cathodes. However, the flammability of their electrolytes remains a significant safety concern.

Na all-solid-state batteries (NaSSBs) have emerged as a safer technology that uses nonflammable and nonvolatile inorganic solid electrolytes (SEs), significantly reducing the risk of thermal runaway.[1,2] However, the practical application of NaSSBs faces significant obstacles due to the low capacity and energy density resulting from the electrode selection, low initial Coulombic efficiency (ICE), and poor cycling stability.[3,4] The hard carbon (HC) anode widely used in SIBs exhibits limited capacity, typically ≈250–320 mAh g^{-1}, and a low volumetric energy density attributable to its low tapped density, often less than 1 g cm^{-3}. In addition, SEs must be added to the anode composite to form an ionic conducting pathway, reducing its energy density and increasing costs.[5–7] Therefore, developing a high-capacity anode is essential for boosting the energy densities of NaSSBs.

Na metal anode is appealing in NaSSBs due to its high capacity and lowest potential. However, it is incompatible with most SEs, leading to detrimental issues such as persistent degradation reactions, dendritic growth, and low critical current density.[8–10] Na-containing alloys, such as sodium-tin (Na-Sn) alloy (e.g., Na_9Sn_4), are confronted with stability issues when exposed to ambient air, which poses significant challenges during fabrication processes. In contrast, Na-free alloy anodes such as Sn offer a notably higher capacity (847 mAh g^{-1})[11] and a high volumetric density of 7.3 g cm^{-3},[12] making them attractive for high energy density full cells. Moreover, the Na-free alloy anode demonstrates environmental compatibility and stability under atmospheric conditions, mitigating challenges associated with anode fabrication. Additionally, alloy-type anodes can function without needing SEs and carbon additives due to their inherent electronic conductivity and Na^+ diffusivity.[13,14] This property not only enhances cell energy density but also reduces the production costs of NaSSBs, making them more economically viable and sustainable for large-scale manufacturing.

Despite the advantages above, NaSSB full cells with alloy anodes often experience inevitable Na^+ loss after the first charging/discharging cycle due to Na^+ trapping in the anode and forming anode/electrolyte interphases. This results in low ICE and

W. Tang, D. Xu, D. J. Lee, A. Fuqua, F. Li, Y. Jeon, Z. Chen
Aiiso Yufeng Li Department of Chemical and Nano Engineering
University of California
La Jolla, San Diego, CA 92093, USA
E-mail: zhc199@ucsd.edu
J. Wu, Z. Chen
Program of Materials Science and Engineering
University of California
La Jolla, San Diego, CA 92093, USA
W. Bian
Energy and Environment Science and Technology
Idaho National Laboratory
Idaho Falls, ID 83415, USA
Z. Chen
Sustainable Power and Energy Center
University of California
La Jolla, San Diego, CA 92093, USA

The ORCID identification number(s) for the author(s) of this article can be found under https://doi.org/10.1002/aenm.202405678

DOI: 10.1002/aenm.202405678

considerably reduced energy density and cycling stability due to an unbalanced negative/positive (N/P) ratio in full cells. In this regard, the presodiation (pre-Na) strategy is crucial to mitigate the initial capacity loss, which can be realized by either anode pre-Na or cathode pre-Na methods.[15–19] Anode pre-Na materials (e.g., Na metal,[17,20] biphenyl/tetrahydrofuran)[21] often exhibit a low potential and high chemical reactivity, akin to typical Na-containing alloy anodes. This method introduces significant manufacturing complexities and raises safety concerns, making their large-scale production impractical. Conversely, cathode pre-Na methods involve the addition of Na-rich additives into the cathode composites, offering the advantages of precise regulation of pre-Na capacity and compatibility with the widely used anode/cathode systems. The effectiveness of this method hinges on carefully selecting a high-capacity pre-Na agent to maximize the overall cell energy density. When designing pre-Na agents, three fundamental requirements should be considered. First, the pre-Na agent should exhibit significantly higher capacities than cathode materials, which is crucial for enhancing capacity. Second, it should ensure controlled Na^+ transport behavior below the charge cutoff voltage and avoid further reduction in the discharge potential range of the cathode. Third, the addition and decomposition of the pre-Na agent should not have detrimental effects such as impeding Na^+ transportation or releasing gases, which are crucial for maintaining stable and efficient battery performance over multiple charging/discharging cycles.

Research on sacrificial pre-Na additives has primarily focused on liquid-based systems, with relatively little exploration within NaSSBs.[22–26] Besides, many of these pre-Na agents exhibit electronic and ionic insulating properties. While this characteristic might not significantly impact liquid battery systems due to the good wettability and high ionic conductivity of liquid organic electrolytes, it is detrimental in NaSSBs. For example, one promising pre-Na candidate is Na_2S, which meets all the design requirements. However, its ionic insulating nature ($\approx 10^{-11}$ S cm^{-1}) could impede Na^+ transport, leading to poor redox kinetics and low Na donation capacity in all-solid-state battery architectures. This situation underscores the need to activate Na_2S as a pre-Na agent for NaSSBs.

Herein, we introduce a cathode pre-Na strategy by activating Na_2S within a composite of Na_3PS_4 (NPS) and acetylene black (AB) (Na_2S-NPS-C), in which NPS serves as the ionic conductor. At the same time, AB provides the necessary electronic conductivity. The composite's electronic conductivity reaches $\approx 10^{-3}$ S cm^{-1}, and the ionic conductivity improves from the order of $\approx 10^{-11}$ (for Na_2S) to $\approx 10^{-5}$ S cm^{-1} (for the composite). An optimal NPS: Na_2S mass ratio (1:2) yields the highest first cycle charge capacity of 511.7 mAh g^{-1}, corresponding to 90% of its theoretical capacity. When implemented in a $NaCrO_2$ (NCO) || Sn full cell configuration, the capacity (based on cathode mass) can increase from 90.8 to 118.2 mAh g^{-1} by adding only 3 wt.% of the pre-Na agent. After 1st cycle activation, no gas was released, and only ≈1.7 wt.% of the inactive material remained in the cathode. Moreover, enhanced cycling performance was confirmed due to the continuous extraction of Na^+ from pre-Na agent residue in the following cycles. As a result, the NCO||Sn full cell with cathode pre-Na agent shows significantly enhanced cycling performance with capacity retention of 90.4% after 300 cycles, far superior to 80.5% for cells without the pre-Na agent. The efficacy of this pre-Na technique in augmenting battery performance was also demonstrated in other cathode/anode combinations, including $Na_xNi_{1/3}Fe_{1/3}Mn_{1/3}O_2$ (NFM) cathode and Sb anode, showcasing its potential for broad applications across various NaSSB chemistries.

2. Results and Discussion

2.1. The Na Loss in the Alloy-Type Anode

To comprehensively evaluate the Na^+ transport and kinetic characteristics in the Sn anode, a galvanostatic intermittent titration technique (GITT) test was conducted at 0.05 C, involving a charging/discharging period of 0.5 h followed by a 2-h rest interval. **Figure 1b** illustrates the voltage profile during the first cycle of the Sn anode. The profile reveals a series of alloying processes of the Sn anode during sodiation (discharging step for Sn || Na_9Sn_4 half-cell), marked by the sequential formation of Na_1Sn_1, Na_9Sn_4, and $Na_{15}Sn_4$ phases, which are characterized by distinct voltage plateaus. For the subsequent desodiation (charging step for Sn || Na_9Sn_4 half-cell) process, the $Na_{15}Sn_4$ alloy transforms back to Na_9Sn_4 and Na_1Sn_1 with significant hysteresis. However, the rest of Na (≈0.8 mol of Na per Sn) remains trapped within the anode due to the slow Na^+ diffusion kinetics of the Na-Sn alloy at low Na content, which was also revealed by the evolution of the Na^+ diffusion coefficient as shown in Figure 1c. Initially, the diffusion coefficient of the pristine Sn anode is $\approx 2\times10^{-6}$ cm^2 s^{-1}. As Na begins to alloy with Sn at a potential of ≈0.40 V (vs Na_9Sn_4, the same below), the Na_1Sn_1 phase is formed, and the Na^+ diffusion coefficient drops sharply to $\approx 10^{-9}$ cm^2 s^{-1}. This drastic decrease reflects the slow kinetic properties of the Na-Sn alloy at low Na content. As sodiation progresses, the formation of the Na_9Sn_4 phase at the second plateau at 0.08 V is accompanied by an increase in the diffusion coefficient ($>10^{-7}$ cm^2 s^{-1}), indicating enhanced transport properties compared to the Na_1Sn_1 phase. At the end of the sodiation step, the $Na_{15}Sn_4$ phase was formed with the potential decreases to −0.13 V. A moderate Na^+ diffusion coefficient of $\approx 10^{-7}$ cm^2 s^{-1} was obtained at this stage. For the desodiation (Na^+ extraction) process, a similar Na^+ diffusion coefficient, ranging from high to low Na content, was observed at each stage of the Na–Sn alloy. As Na extraction nears the completion of the Na_1Sn_1 phase, the diffusion coefficient rapidly declines to $\approx 10^{-10}$ cm^2 s^{-1}, indicating difficulty in removing the remaining Na. Consequently, some Na becomes irreversibly trapped within the anode, leading to permanent Na loss. Figure 1d shows the X-ray diffraction (XRD) pattern of the Sn anodes after charging/discharging in the half-cell to identify the composition of the products. The characteristic peaks of $Na_{15}Sn_4$ and Na_9Sn_4 were detected from the fully sodiated electrodes. After desodiation, the XRD pattern showed a strong signal of the Na_1Sn_1 phase and lower Na^+ content of $NaSn_2$. Joshua et al. calculated the formation enthalpy per atom versus Na concentration in the Na–Sn compound and constructed the convex hull to show the stable structures.[27] The results show that compared with pure Sn, Na_1Sn_1 has a lower formation energy, ≈−0.02 eV per atom, which results in a barrier for Na to return to the cathode during discharge. Such alloying components as discharged products were also observed in earlier works.[28,29]

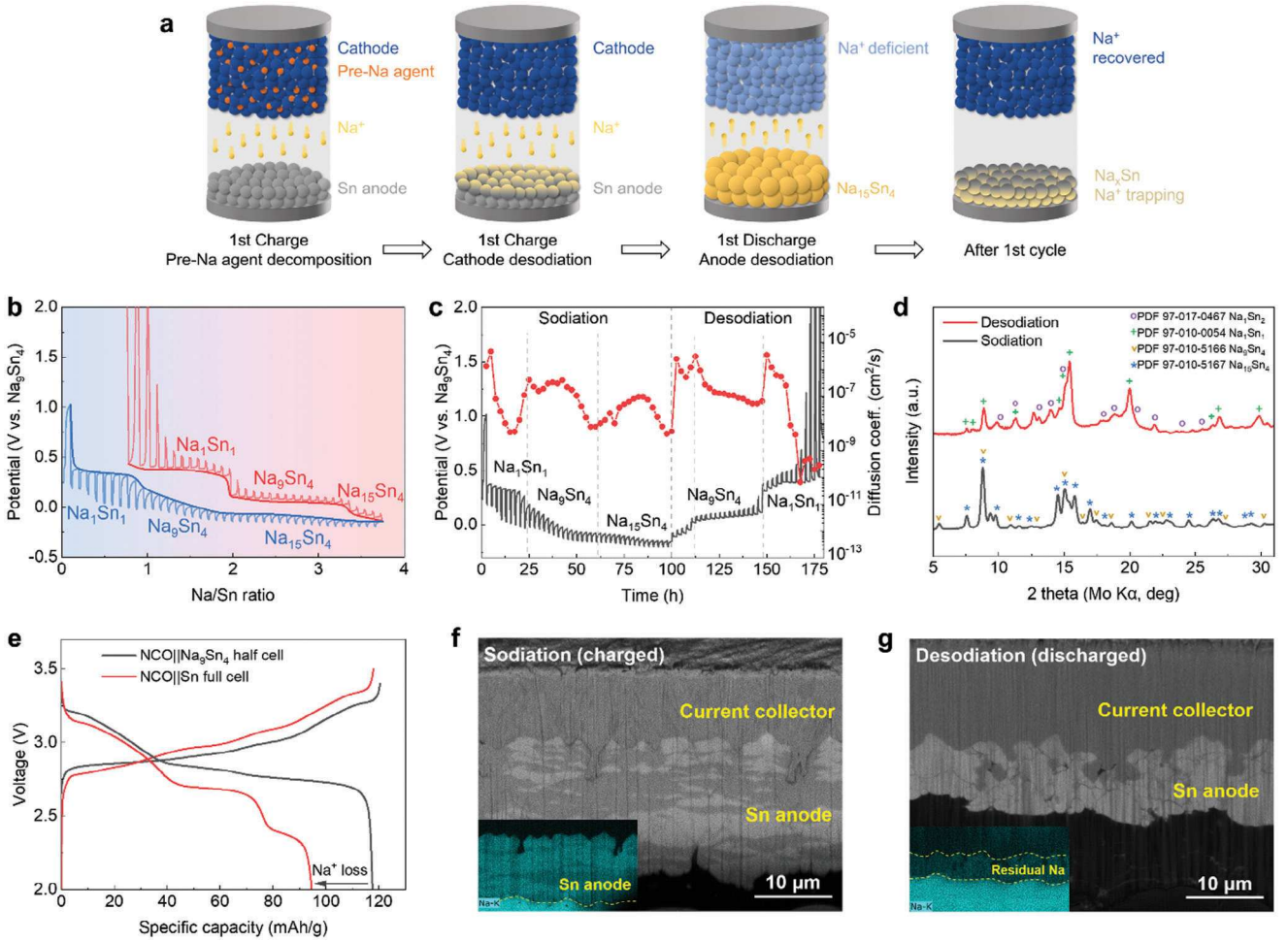

Figure 1. Characterizations and mechanism study of Na^+ loss in NaSSB full cell with Sn anode during the 1st cycle. a) A scheme of cathode presodiation strategy used to compensate for Na trapping in the Sn anode and avoid Na loss in the cathode. b) Charge/discharge GITT voltage curves of Sn||Na_9Sn_4 half-cell to show phase transition of Sn alloy anode and Na^+ trapping in the first cycle. c) Na^+ diffusion coefficient in different phases of Na-Sn alloy determined by GITT. d) XRD patterns of Na-Sn alloy after the 1st cycle of sodiation and desodiation. e) The 1st cycle charge/discharge curve of the NCO||Sn full cell and the NCO||Na_9Sn_4 half-cell to illustrate their differences in ICE and highlight Na^+ trapping in the full cell. f) SEM images and EDX mapping of the Sn anode after the initial sodiation and g) desodiation process.

The NCO || Na_9Sn_4 half cells and NCO || Sn full cells were tested to elucidate the Na loss phenomena, as shown in Figure 1e. For the NCO || Na_9Sn_4 half-cell, a high capacity of 117.5 mAh g^{-1} and a high ICE of 97.61% was achieved. In contrast, a lower capacity of 94.6 mAh g^{-1} and ICE of 80.6% were achieved for the NCO || Sn full cell. In the NCO || Na_9Sn_4 half-cell, the excess Na inventory in the Na_9Sn_4 counter electrode facilitates the restoration of Na stoichiometry in the NCO cathode, leading to a high ICE. Conversely, in the NCO || Sn full cell, a significant portion of Na^+ becomes trapped within the Sn anode during the alloying process, resulting in a much lower ICE.

To study the morphology evolution and Na distribution, Figure 1f,g show the focused ion beam milling-scanning electron microscopic (FIB-SEM) images and energy dispersive X-ray spectroscopic (EDX) mapping of the Sn anode in the full cell at the charged and discharged states, respectively. After charging (Figure 1f), the Sn anode alloys with Na and experiences apparent volume expansion. The observed striped structure could be attributed to the different phases of Na-Sn alloy due to a nonuniform sodiation reaction. The EDX mapping of Na shown in the cyan areas suggests a higher Na concentration within the charged anode. After discharging, the particles contract when Na^+ is removed from the alloyed anode, with the thickness reduced from ≈16.1 to ≈6.8 μm. While most of the Na is removed, a significant amount remains at the anode as shown in the EDX image, indicating irreversible Na trapping.

The trapped Na results in a Na deficiency in the cathode, structural changes, and degradation in both the cathode and anode over subsequent cycles, leading to capacity decay in full cells. Introducing Na-rich additive with a high decomposition capacity to the cathode is logically feasible to compensate for the Na inventory loss due to these reasons. Hence, properly controlling the N/P ratio and the presodiation extent is critical to ensure enough Na in the cathode for stable battery cycling.

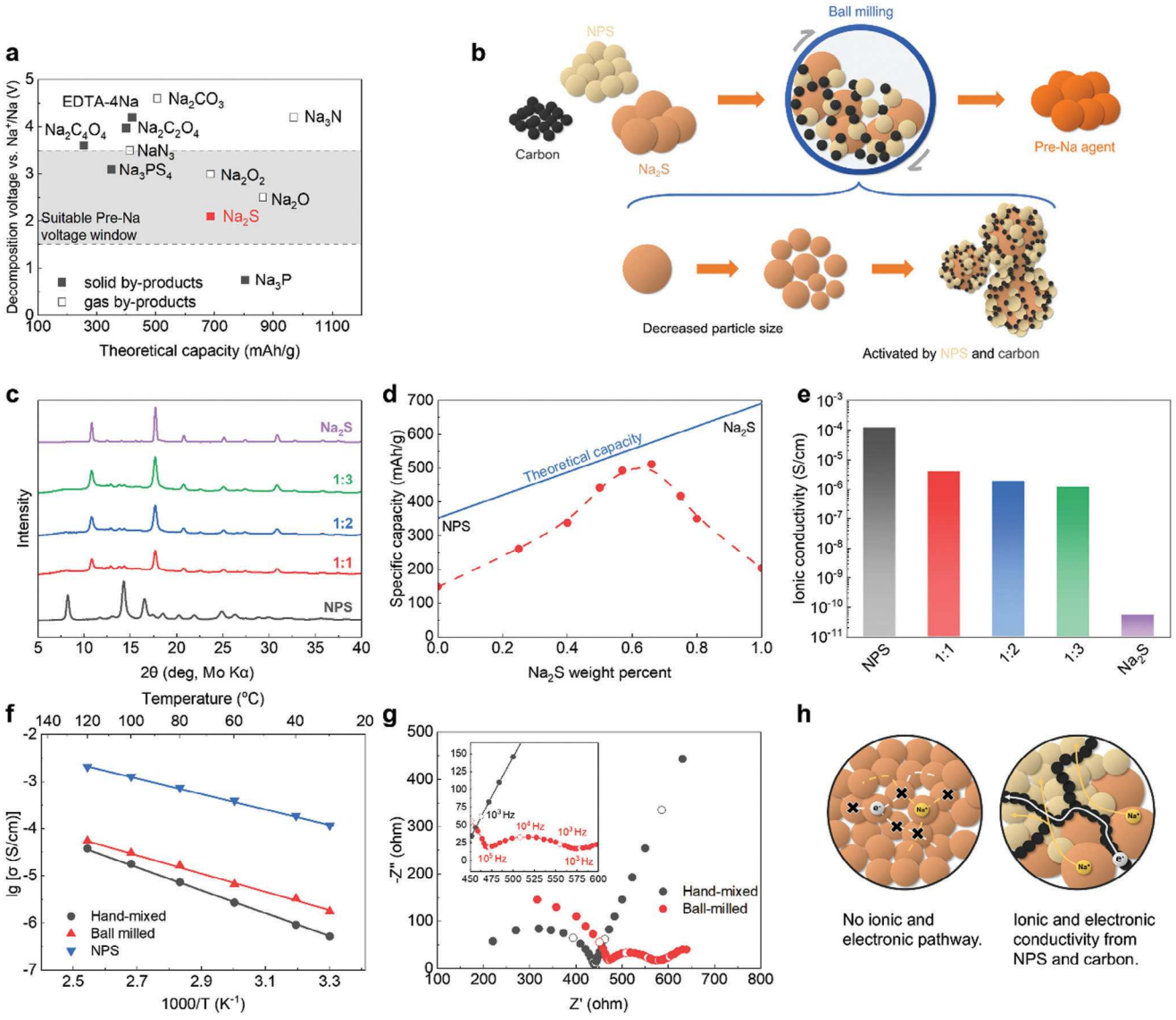

Figure 2. Pre-Na agent design and characterizations. a) The theoretical capacity and the decomposition voltage of the potential cathode additives for presodiation. b) Scheme describing the preparation of the pre-Na agent using ball milling to mix Na_2S, NPS, and AB. c) The XRD patterns of the pre-Na agents with various NPS and Na_2S ratios (NPS: Na_2S) after ball milling. d) Diagram showing the calculated theoretical capacity and the trend of the actual capacity of pre-Na agent with different Na_2S ratios. e) Ionic conductivity of different pre-Na agent compositions. f) The Arrhenius plot of the pre-Na agent was mixed by hand and ball milling to show the conductivity and activation energy. g) Nyquist plots of the hand-mixed and ball-milled pre-Na agent assembled with Na_9Sn_4 as half-cell before charging. h) Scheme to show the pristine Na_2S failing to conduct electrons and Na^+ and its activation by ball milled with NPS and AB to form ionic and electronic pathways.

2.2. Pre-Na Agent Design and Characterization

The theoretical capacity is a primary consideration when selecting pre-Na agents. Composites with heavy anions and more complex structures may not be ideal due to their lower capacities, as shown in Figure S1 (Supporting Information). Pre-Na agents with higher capacities (>500 mAh g^{-1}) are advantageous because they enhance the battery energy density while minimizing the negative impact of introducing additional reaction products.[30–36] In this regard, simple compounds such as sodium nitride (Na_3N), sodium oxide (Na_2O), sodium phosphide (Na_3P), and sodium peroxide (Na_2O_2) exhibit potential (**Figure 2a**). However, for Na_3N, Na_2O, and Na_2O_2, the nitrogen or oxygen gas generated in the decomposition process during the first charging cycle will cause volume expansion and the deterioration of the interface contact, thus increasing impedance and accelerating the cell performance degradation. Although Na_3P boasts a high capacity of 804 mAh g^{-1} with no gas release, its low decomposition voltage (<1 V vs Na/Na^+) is incompatible with the electrochemical stability window of the widely used halide and sulfide SEs.[37,38] This incompatibility triggers reactions with SEs and the formation of insulating products, which significantly decrease the ionic conductivity, escalating the battery resistance and impedance.

In contrast, Na_2S emerges as a more promising pre-Na agent with a moderate decomposition voltage (≈1.8 V) and a high theoretical capacity of 687 mAh g^{-1}. Unlike nitrides and oxides, its decomposition yields only elemental sulfur without gas production, avoiding volume expansion and gas-related degradation. Nevertheless, pure Na_2S suffers from extremely low ionic conductivity (σ_{Na+}) of 5.4×10^{-11} S cm^{-1} (Figure S2, Supporting Information) and is almost electronically insulating, which hinders its electrochemical oxidation and the Na^+ extraction during charging.[39] To overcome these limitations, it is essential to create ionic and electronic transport pathways that facilitate the electrochemical decomposition of Na_2S. Here, we introduced NPS to activate Na_2S for pre-Na due to their similar chemical compositions. As a widely used SE in NaSSBs, NPS offers a notably high ionic conductivity (1×10^{-4} to 2×10^{-4} S cm^{-1})[40,41] with an oxidation voltage of ≈2.5 V.[42–44] This is higher than the decomposition voltage of Na_2S but lower than typical cathode operation voltage (e.g., NCO, NFM), making it an ideal choice for activating Na_2S with minimal impact. The higher desodiation voltage of NPS allows Na_2S to contribute Na^+ at a lower voltage, followed by Na^+ extraction from NPS itself, maximizing its capacity utilization. After the decomposition of NPS, there is a decrease in ionic conductivity for the pre-Na agent, which prevents Na^+ from returning and ensures the irreversible pre-Na process.

Therefore, we designed Na_2S-NPS-C pre-Na composites, which were synthesized by simple ball milling. The effects of ball milling and the varying ratios of Na_2S and NPS in these composites were investigated. A scheme describing ball milling to obtain the pre-Na agent is shown in Figure 2b. The large particles of Na_2S were fragmented into smaller sizes during the ball milling process and combined with NPS particles and AB to obtain a higher ionic and electronic conductivity as a composite. Figure 2c shows the XRD patterns of Na_2S, NPS, and synthesized pre-Na composites. After ball-milling, pre-Na agents exhibit identical peaks of Na_2S with increased peak intensity for higher Na_2S content in pre-Na agents. The weak NPS peak indicates that the crystalline NPS was converted into an amorphous phase after the ball-milling process.[45] Meanwhile, the Na_2S peak was broadened, indicating the grain size reduction.

The initial charging capacity of pre-Na with different Na_2S and NPS ratios is tested in a cell configuration of pre-Na agent || NPS || Na_9Sn_4 (Figure 2d), and their charging voltage profiles are depicted in Figure S3 (Supporting Information). The theoretical capacity of the pre-Na agent was calculated based on the total Na^+ content in the composition (total mass of Na_2S and NPS) (Equation (1)):

$$C_t = \lambda_{Na_2S} \times C_{Na_2S} + \lambda_{NPS} \times C_{NPS} \quad (1)$$

where C_t is the theoretical capacity of the pre-Na agent; λ_{Na_2S} and λ_{NPS} are the mass ratio of Na_2S and NPS in pre-Na agent, respectively; C_{Na_2S} and C_{NPS} are capacity for Na_2S (687 mAh g^{-1}) and NPS (352 mAh g^{-1}), respectively.

After ball milling with AB, pure NPS exhibits a capacity of 148.8 mAh g^{-1} after being charged to 4 V, achieving only 42.3% of the theoretical value. This insufficient decomposition is likely due to the poor kinetics from the continuous decrease in σ_{Na+} along with the process of Na^+ extraction. The charging curve for pure NPS is a continuous sope, with no plateau at any specific voltage. As the Na_2S content increases, the Na^+ donation capacity rises dramatically due to the substantial release of Na^+ from Na_2S. The highest charge capacity of 511.7 mAh g^{-1} was achieved at the mass ratio of NPS: Na_2S at 1:2, corresponding to an approximate molar ratio of 1:6. The theoretical capacity for this composition is estimated to be ≈575.3 mAh g^{-1}, indicating that near 90% of the Na^+ are utilized during 1st charging. However, a capacity decrease is observed when the Na_2S ratio increases beyond this point. Only 417.5 mAh g^{-1} was obtained at the ratio of NPS: Na_2S at 1:3. This reduction in capacity can be attributed to the decreased volume ratio of NPS electrolytes leading to poor percolation network for Na^+ conduction. The differential capacity (dQ/dV) curve (Figure S4, Supporting Information) reveals the reaction plateaus of each composite ratio, with two characteristic peaks appearing at ≈2.0 and 2.3 V, corresponding to the two stages of the phase transformation of the Na_2S during the decomposition. At the end of the 1st stage at 2.1 V, the 1:2 ratio sample achieves a capacity of 259.5 mAh g^{-1}, ≈60% of the Na_2S theoretical capacity. This indicates an intermediate product of polysulfide Na_2S_x was generated.[46] In the 2nd stage, Na_2S_x continuously loses Na, contributing to the remaining charge capacity. However, without mixing with NPS electrolyte, the peak intensity in the 2nd stage of the Na_2S-AB mixture is inapparent (Figure S4, Supporting Information). Due to the low σ_{Na+} of Na_2S, it is difficult to fully activate Na_2S by further extracting Na^+, leading to a much lower capacity. Therefore, sufficient NPS is critical to maintain ion transport pathways within particles to fully extract the Na^+ capacity of the pre-Na agents.

To reveal the electrochemical properties of the pre-Na composites with various ratios, their σ_{Na+} and electronic conductivities (σ_e-) were measured and compared to quantitatively dissect the role of NPS and AB. The σ_{Na+} of Na_2S-NPS-C composites were measured by the DC polarization method using a symmetrical cell (Na_9Sn_4 || NPS || Na_2S-NPS-C || NPS || Na_9Sn_4) as illustrated in Figure S5a (Supporting Information). The NPS layers function as electronic block layers, and their resistance was subtracted when calculating σ_{Na+} of the pre-Na agent. The Na_9Sn_4 alloy added on each side was a Na source and current collector. The σ_{Na+} of the pre-Na agent with different NPS: Na_2S ratios were determined from the obtained value after applying a 0.1 V bias voltage for 300 s, which shows a much-improved σ_{Na+} than pure Na_2S and an increasing trend with a higher NPS ratio as shown in Figure S5b (Supporting Information). Specifically, the σ_{Na+} was 3.9×10^{-5}, 1.8×10^{-5}, and 1.2×10^{-5} S cm^{-1} for composites with NPS: Na_2S mass ratio of 1:1, 1:2, and 1:3, respectively (Figure 2e). The σ_e- of pure Na_2S is extremely low, which behaves as an electronic insulator. However, after ball milling with AB, the σ_{e-} was improved to 1.3×10^{-2}, 1.8×10^{-2}, and 2.8×10^{-2} S cm^{-1} for the respective NPS: Na_2S ratios (Figure S6, Supporting Information). Compared with the σ_{Na+} of the pre-Na agents, their σ_e- were nearly three orders of magnitude higher, which indicates that ionic conductivity is the main factor limiting charge transfer and capacity utilization. The NPS: Na_2S = 1:2 mixture with the highest specific Na^+ capacity was selected for further analysis.

To understand the impact of the ball-milling process, the ionic conductivities of samples prepared by ball-milling and hand-mixing were measured at different temperatures to construct an Arrhenius curve. As shown in Figure 2f, the ball-milling samples exhibited higher ionic conductivity (about one magnitude)

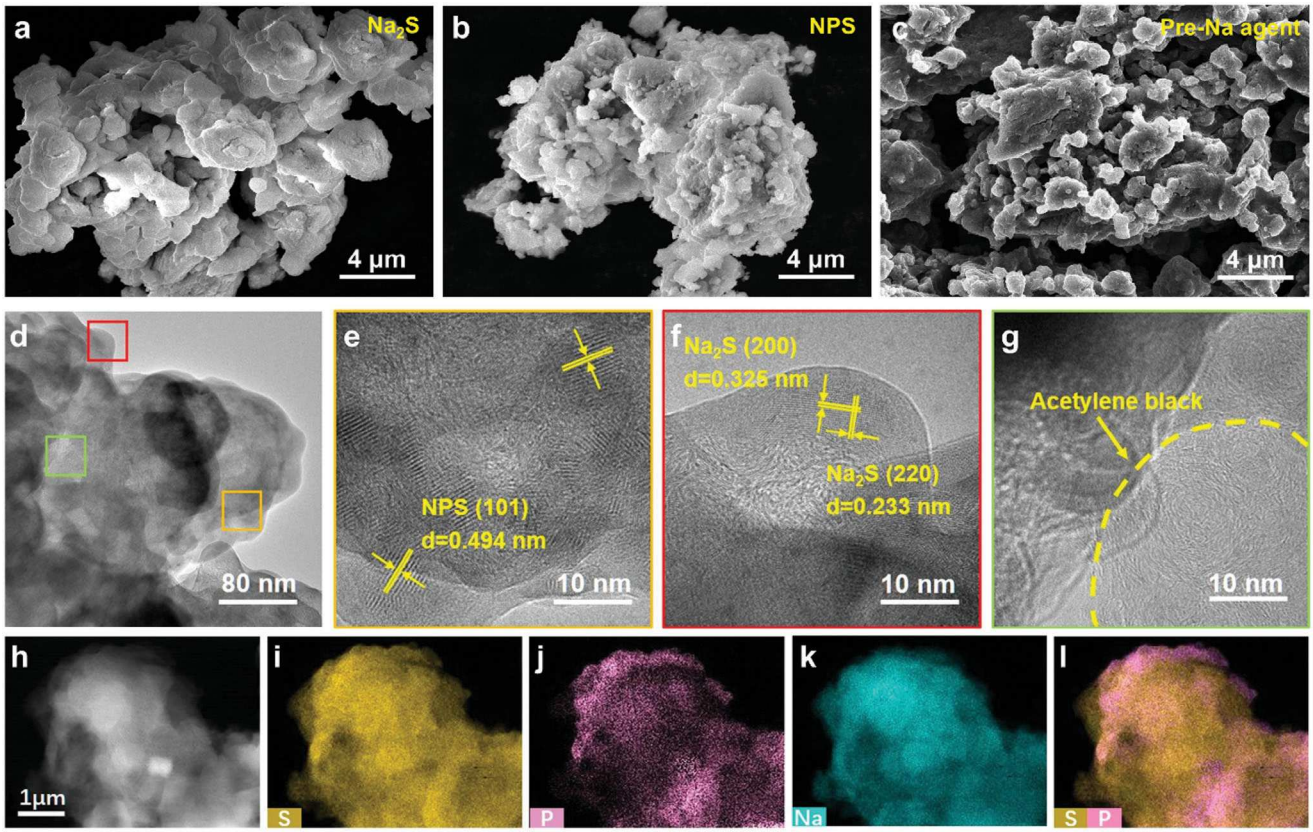

Figure 3. Characterization of the particle morphology and structure of the pre-Na agent. a–c) The SEM image of the Na_2S, NPS, and the pre-Na agent. d) The cryo-TEM image of the pre-Na agent particles after ball milling. e–g) The partially magnified photos of the particular area showing the NPS, Na_2S particle, and AB structure. h–l) STEM EDX mapping of a single pre-Na agent particle to show the elemental distribution of S, P, Na, and a mixture of S and P to compare.

across all temperatures compared to the hand-mixing samples, with a lower activation energy (0.35 vs 0.44 eV). Both samples were assembled into half-cells with Na_9Sn_4 for electrochemical impedance spectroscopy (EIS) measurement. Figure 2g indicates that the hand-mixing sample exhibits no electrochemical activity. In contrast, the ball-milling sample showed an R_p of ≈107 Ω, with the characteristic peak frequency of 10^4 Hz. This difference suggests that ball milling is essential to activate Na_2S by forming a conductive pathway for ions and electrons between the particles (Figure 2h).

SEM and cryogenic transmission electron microscopy (cryo-TEM) with EDX were utilized to characterize NPS and carbon distribution within the pre-Na agent composites. The pristine Na_2S and NPS particles exhibit sizes ≈3.5 and 1.5 μm, respectively (**Figure** 3a,b). After the ball milling process, the large Na_2S particles were reduced into smaller particles at ≈1.5 μm, and the softer sulfide NPS particles were ground and dispersed around the Na_2S particles (Figure 3c,d). The SEM-EDX mapping of the pre-Na agent (Figure S7, Supporting Information) demonstrates a uniform elemental distribution of S, P, Na, and C. Cryo-TEM shows lattice fringes with a spacing of 0.494 nm, corresponding to the (101) lattice of crystalline NPS (Figure 3e). Distances of 0.325 and 0.233 nm are directed toward the (200) and (220) directions of Na_2S, respectively, with these characteristic fringes filling most of the field of view as the primary phase (Figure 3f). Cluster-like fringe structures can be observed, corresponding to typical carbon structures from the AB in the pre-Na agent. EDX mapping of a single particle of pre-Na composite reveals that NPS (characterized by the P signal) and Na_2S are well-mixed in particle scale after ball milling. This shows the structural characteristics of the pre-Na agent and elucidates the mechanism of using NPS and AB to improve ion/electron conductivity.

2.3. Electrochemical Performance

Figure 4a presents the charge and discharge profile of the NCO cathode and the pre-Na agent in the voltage window of 2.25 to 3.5 V. The NCO cathode exhibited a capacity of 117.5 mAh g^{-1}, while the pre-Na agent exhibited a significantly higher charging capacity of 511.7 mAh g^{-1} with a negligible discharge capacity in the same voltage range. This property meets the requirement that after the pre-Na agent releases its stored Na^+ during the cathode charging process, it does not take in Na^+ during discharging. Further investigation was conducted on NCO cathode composites containing 60 wt.% of active material and 1, 2, and 3 of pre-Na agent (Figure 4b). After aligning them to the same capacity,

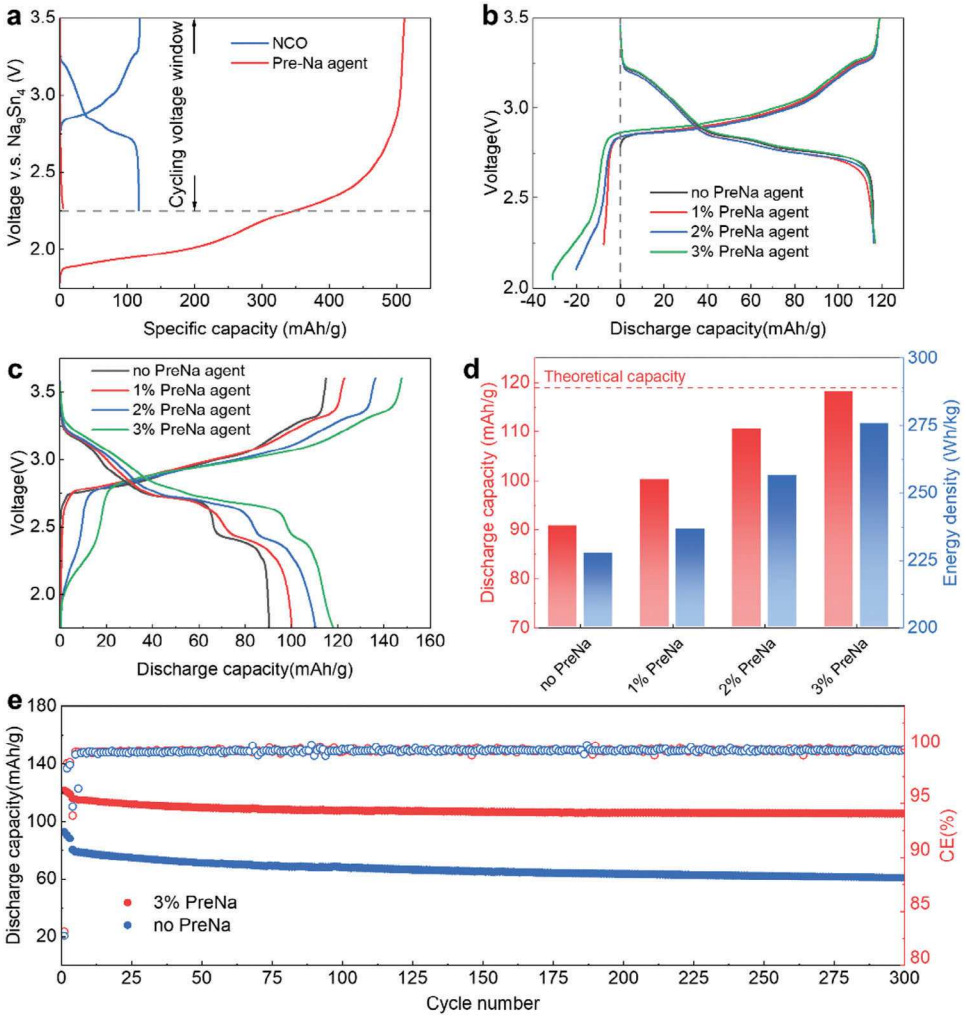

Figure 4. Electrochemical characterization of the NCO cathode composite with pre-Na agent added. a) Comparison of charging and discharging voltage curves between NCO cathode and pre-Na agent. b,c) Charge and discharge curves of the first cycle of NCO||Na_9Sn_4 half-cell and NCO||Sn full-cell with different pre-Na agent ratios. d) Comparison of cathode discharge capacity and full cell energy density (based on the mass of cathode + anode + pre-Na) after adding the pre-Na agent. e) Long-term cycling performance of the NCO||Sn full cell with/without pre-Na agent.

it was observed that Na^+ is extracted from the pre-Na agent before reaching the NCO charging plateau. Adding 3 wt.% of pre-Na agent to the composite increased the charging capacity from 119.0 mAh g^{-1} (w/o pre-Na agent) to 150.2 mAh g^{-1}. All cells displayed similar discharge capacities, indicating that the extra Na^+ transferred from the cathode is accumulated at the anode side.

We then tested NCO cathodes with and without the pre-Na agent in an NCO||Sn full cell with an N/P ratio of 1.1 and a voltage window of 1.75 to 3.6 V (Figure 4c). All these cells show a similar ICE of ≈80% (Figure S8, Supporting Information), while their discharge capacity increases with more pre-Na being added in the cathode composite. With 3 wt.% of pre-Na agent, the discharge capacity of the NCO||Sn full cell increased from 90.8 to ≈118.2 mAh g^{-1}, similar to the NCO||Na_9Sn_4 half-cell, which corresponded to a 30.2% increase in capacity. This translates to a 21% increase in energy density based on the total weight of the cathode, anode, and pre-Na agent (Figure 4d). The full cell with the pre-Na additive also demonstrated stable cycling and significantly enhanced capacity retention (**Figure 5e**). After 300 cycles at 0.5 C, the capacity retention of the full cell without pre-Na was 80.5%, while the cell with 3% pre-Na agent achieved a 90.4% capacity retention. This suggests that even though most of Na^+ has been extracted, the residual Na^+ in the pre-Na agent acts as a "Na^+ reservoir" that may continuously compensate for the Na^+ loss during the cycling, thereby enhancing cycling stability.[47]

2.4. The Pre-Na Mechanism

Figure 5a,b display the SEM images of the post-charging cathode, observed from the surface and cross-section, respectively. Under backscattering mode, dark spots were randomly dispersed within the cathode composite. EDX reveals that these areas contain sulfur (S) and phosphorus (P)-rich species, suggesting they are residues of pre-Na.

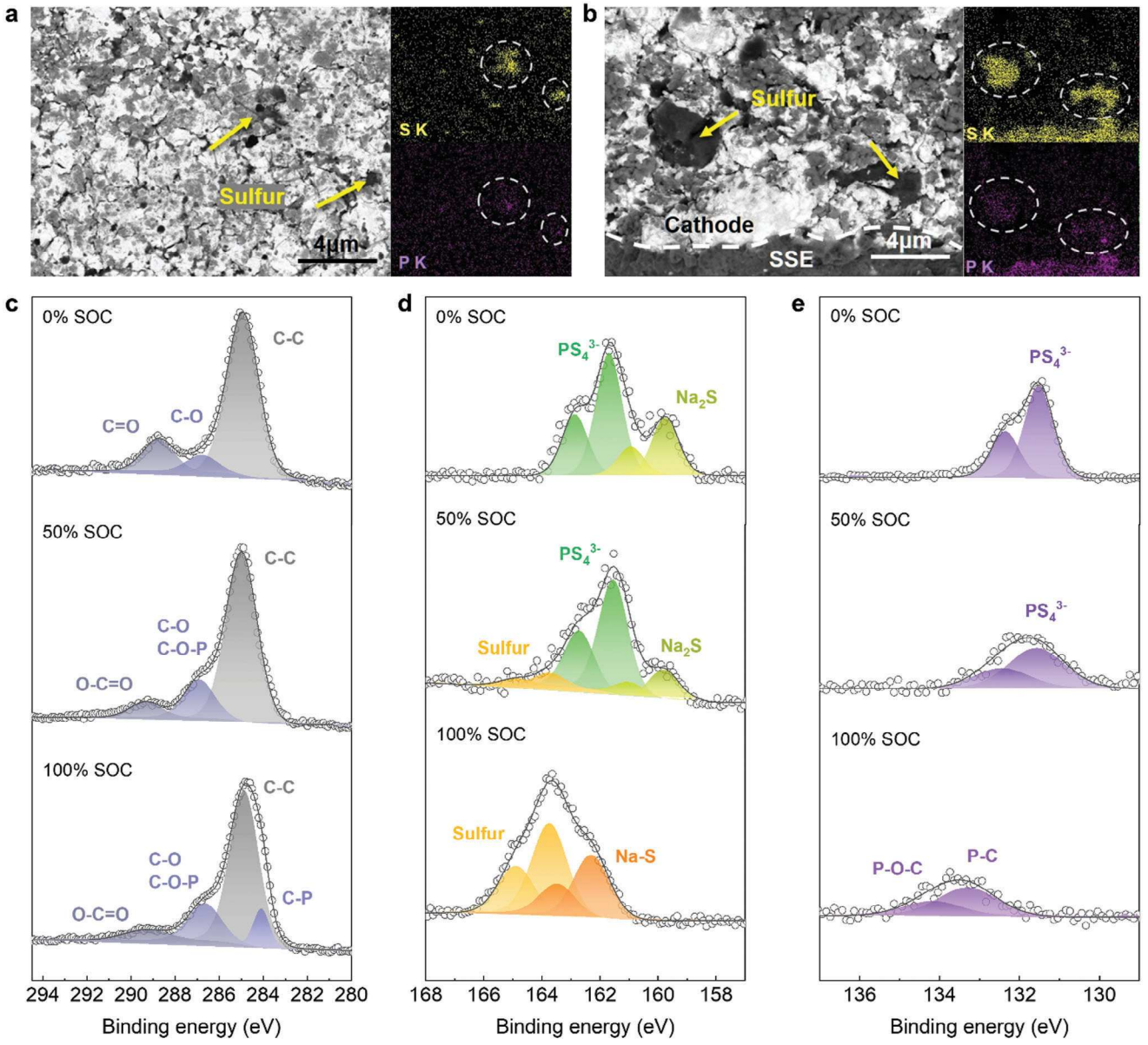

Figure 5. Structure and composition evolution of the cathode composite during the charging process. a,b) SEM images (backscattered mode) and EDX mapping of the cathode from the post-mortem cell showing a) the surface and the cross-section. c–e) XPS analysis of the C 1s, S 2p, and P 2p elements to characterize the change of chemical composition at different states of charge (SOC).

X-ray photoelectron spectroscopy (XPS) was used to determine the composition of these species. In the pristine pre-Na agent, the C—C bond seen in the C_{1s} spectrum (Figure 5c) indicates the presence of carbon (AB). The S 2p spectrum (Figure 5d) reveals distinctive PS_4^{3-} peaks relating to NPS at 161.6 eV and Na_2S at 159.6 eV.[48,49] The P 2p spectrum (Figure 5e) also displays a PS_4^{3-} peak at 131.4 eV.[50] At the charging step, the decomposition of Na_2S is proved by the reduction of its peak intensity and the appearance of new peaks at 163.8 eV. This indicates the formation of elemental S as the final product.[51–53] Concurrently, the peak intensity of PS_4^{3-} decreases in both the S 2p and P 2p spectra, further confirming the decomposition of NPS. By the end of the charging process (100% SOC), the peaks for Na_2S and PS_4^{3-} are no longer detectable. A significant increase in the S peak and a new peak at 162.4 eV are observed, reflecting the formation of Na-S bonds and the polysulfide compound (Na_2S_n) from Na_2S decomposition.[50,54,55] Simultaneously, the P 2p spectrum shows new peaks at 133.2 and 134.2 eV, corresponding to the oxidized product P_2S_5.[56]

EIS and distribution of relaxing time (DRT) were used to analyze the decomposition process of the pre-Na agent at different SOCs. The cell was charged at 0.1 C and paused for an EIS test per hour (Figure S9, Supporting Information). In the entire charging process, the cell Ohmic resistance (R_Ω) was maintained at ≈480 Ω (Figure S10a, Supporting Information), indicating no electrolyte-related degradation. As the SOC increases from 0% to

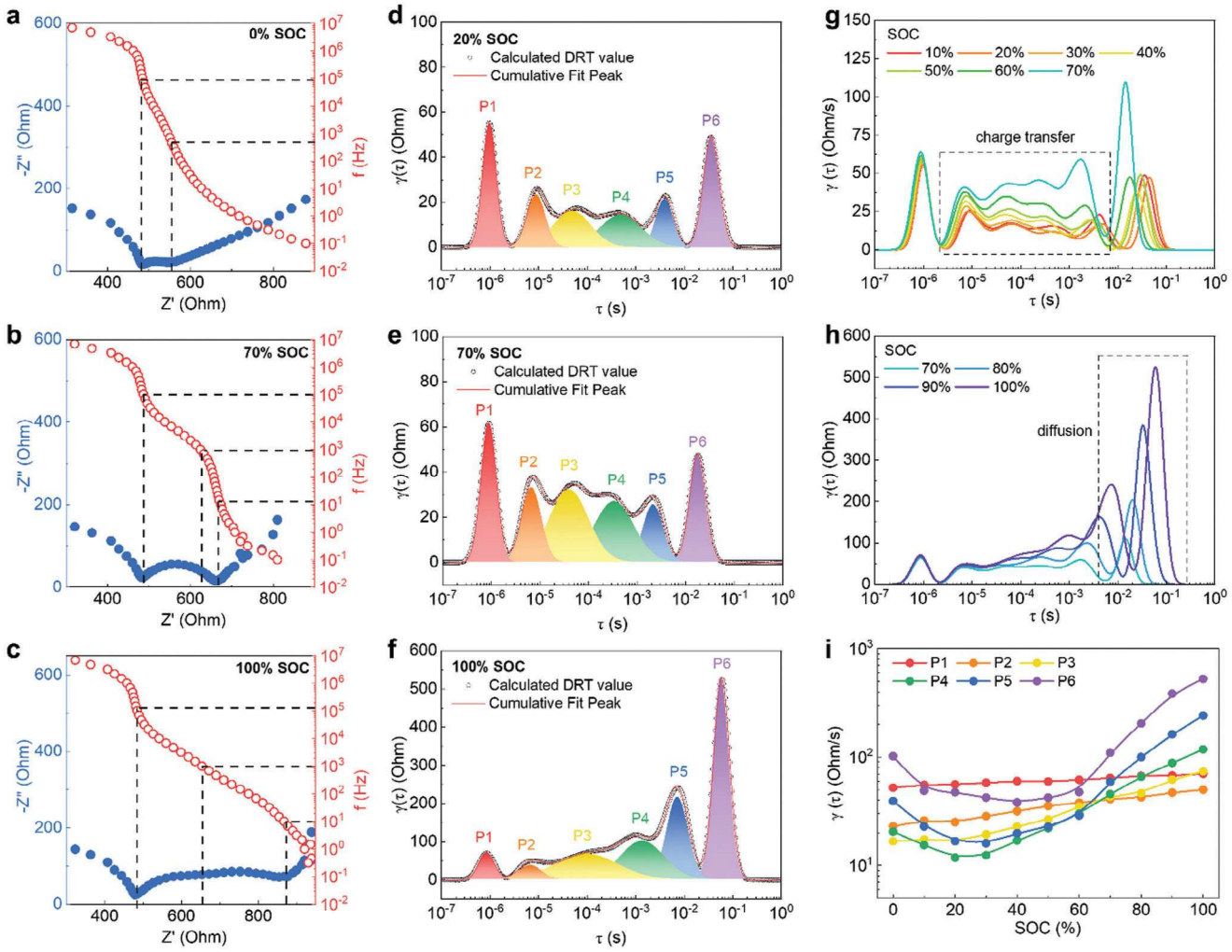

Figure 6. The evolution of the cathode composite impedance with the pre-Na agent during the 1st charging process. a–c) Nyquist plots of the cells with pre-Na agent as the cathode at SOC of 0%, 70%, and 100%, respectively. d–f) DRT results derived from the Nyquist plots with peaks fitted at different SOC (20%, 70%, and 100%) to show multiple electrochemical processes. g) A comparison of the DRT curves at SOC from 10% to 70% and h) 70% to 100%. i) All peak intensity evolution with SOC from 0% to 100%.

70% (**Figure 6**a,b), the polarization resistance R2 (the equivalent circuit in Figure S10b, Supporting Information) of the battery rose from 61.4 to 181.9 Ω, which relates to the charge-transfer reactions with the characteristic frequency at ≈10^5 to 10^3 Hz. This corresponds to the continuous extraction of Na^+ from Na_2S. When SOC is higher than 70%, a new semicircle with a characteristic frequency at 10^3 to 10^1 appears (R3/CPE3), indicating that NPS starts to decompose and leads to slower Na^+ transportation kinetics inside pre-Na particles. As the Na^+ was further extracted from the pre-Na agent, R3 increased dramatically (Figure 6c), resulting from the NPS decomposition and the depletion of Na^+ from pre-Na.

The DRT curves corresponding to different SOCs are shown in Figure 6d–f, which were deconvoluted to six different peaks (P1-P6), corresponding to the dominant electrochemical processes, further elucidating the decomposition process of the pre-Na agent. The P1 peak, with a time constant of 10^{-6} s, remains unchanged during the charging process, corresponding to the resistance of Na^+ ions transferred across the SE grain boundaries.[57,58] Peak P2-P4, with time constants ranging from 10^{-5} to 10^{-3} s, are related to the charge transfer processes between the electrode and SE, including both the anode and cathode sides. These peaks gradually increase as the SOC increases from 0% to 70%, as shown in Figure 6g. Given that abundant Na_9Sn_4 alloy is used on the anode side, the increased impedance primarily contributes to the cathode side of the pre-Na agent. As Na^+ is gradually extracted from Na_2S, the intermediate product of polysulfide Na_2S_x has lower electrochemical activity, leading to increased charge transfer resistance. When the pre-Na is further charged to SOC> 70%, peaks P5 and P6 with a time constant from 10^{-3} to 10^{-1} s surge dramatically, with the peak shift to the higher time constant or lower characteristic frequency (Figure 6g,i). These processes are related to diffusion within the pre-Na agent. At this stage, final products of elemental S and P_2S_5 are generated, which impedes Na^+ transfer from the pre-Na. Concurrently, the decomposition of NPS begins to affect the

Na^+ diffusion of the pre-Na agent significantly. The DRT analysis supports the EIS discussion well and is consistent with our XPS results.

To summarize, after the decomposition, the residue materials of polysulfides and elemental sulfur exhibit low conductivity and electrochemical activity. However, since only 1.7 wt.% of residue remains in the cathode composite, it slightly reduces the conductivity and increases the impedance of the whole cathode composite. The small particle size scaling in several micrometers, as shown in Figure 5a,b, will not affect the electrochemical properties of the bulk cathode significantly. The negative influence of the residue inactive materials is negligible when compared with the improvement from the pre-Na agent, especially reflected in the higher retention rate of the long cycle performance as shown in Figure 4e.

2.5. Broad Application of Pre-Na in NaSSBs

Due to the favorable decomposition voltage of Na_2S, this pre-Na agent can be utilized in various NaSSB systems. To demonstrate its broad applicability, we tested it in full cells with $NaNi_{1/3}Fe_{1/3}Mn_{1/3}O_2$ (NFM) cathode and/or an antimony (Sb) anode. Figure S11a–c (Supporting Information) showcases the initial charge and discharge cycles for three full-cell configurations: NFM || Sn, NFM || Sb, and NCO || Sb. The NFM cathode paired with the Sn anode achieved an ICE of 82%, similar to that with the NCO || Sn full cell. Introducing a 3% pre-Na agent to the NFM cathode enhanced the discharge capacity from 111.2 to 132.7 mAh g^{-1}. Cells with Sb anode (NCO || Sb and NFM || Sb) exhibited lower ICEs (≈70%) due to more severe Na^+ trapping associated with Sb anode. Thus, they require a slightly higher amount (5 wt.%) of pre-Na agent to compensate for the increased Na^+ loss to recover the cathode capacity fully. Figure S12 (Supporting Information) provides a standardized calculation method for determining the pre-Na agent ratio. Additionally, this method is extended to accommodate various cathode (e.g., $Na_3V_2(PO_4)_2F_3$ (NVP)) and anode (e.g., hard carbon) materials. Long-term cycling tests showed that these batteries with pre-Na agent maintained over 90% capacity retention after 300 cycles (Figure S11d–f, Supporting Information), highlighting the positive impact of pre-Na agent on battery performance as illustrated in NCO/Sn full cells.

3. Conclusion

This study presents a universal cathode pre-Na strategy to address the first cycle irreversible capacity loss in NaSSBs. Na_2S was used as the Na donor due to its high theoretical capacity, no gas generation, and suitable Na extraction voltage window. The activation of Na_2S was achieved by creating a mixed electron-ion conducting network using NPS and AB. The ball milling process is essential for activating Na_2S, as it significantly reduces the particle size of Na_2S and increases contact with NPS and AB, ensuring a uniform percolation network. The pre-Na agent with the optimal ratio NPS: Na_2S = 1:2 exhibits enhanced σ_{Na+} of 1.8×10^{-5} and σ_e- of 1.8×10^{-2} S cm^{-1}, achieving a high capacity of 511 mAh g^{-1}. By incorporating a small amount of Na_2S-NPS-C pre-Na agent into the cathode, the released Na^+ compensates for anode trapping, allowing the full cell to achieve the theoretical capacity, thereby maximizing energy density and advancing the development of NaSSBs. Additionally, cycling stability is improved due to the gradual release of residue Na^+ from the pre-Na agent, offering significant potential for next-generation high-energy-density batteries.

4. Experimental Section

Material Synthesis—Na_3PS_4 Electrolyte (NPS): Two precursors, Na_2S (Sigma–Aldrich 98%) and P_2S_5 (Sigma–Aldrich 99%) were mixed with a pestle in the mortar. Then, the mixture was transferred into ball milling jars with a total mass of 1 g, sealed with Y-ZrO_2 grinding media under an argon atmosphere. Ball milling was carried out by a ball miller machine (TMAX XQM) proceeding at 700 RPM for 6 h. Na_3PS_4 electrolyte powder was collected after ball milling without further treatment.

Material Synthesis—Presodiation Agent: First, synthesized NPS, Na_2S (Sigma–Aldrich 98%), and acetylene black (Thermo Scientific 99.9%) with the desired mass ratio were manually mixed in the mortar. The mixture was then transferred into ball milling jars and sealed with Y-ZrO_2 grinding media under an argon atmosphere. Ball milling was carried out by a ball miller machine (TMAX XQM) proceeding at 600 rpm for 5 h.

Material Synthesis—Na_9Sn_4: The Na_9Sn_4 alloy was synthesized by ball-milling the sodium block and tin powder. First, the sodium block was manually mixed with the tin powder in the mortar with a pestle until pulverized, forming a powdery sodium–tin alloy. Then the mixture was transferred into ball milling jars and sealed with Y-ZrO_2 grinding media under an argon atmosphere, ball-milled at 500 rpm for 2 h to let the reaction sufficiently happened, and form a uniform sodium-tin alloy.

Materials Characterization: X-ray diffraction (XRD) samples were loaded into glass capillary tubes (Charles Supper) of 0.5 mm diameter inside a glovebox, sealed with clay and wrapped with parafilm. Then, the samples were removed from the glovebox and flame-sealed using a butane torch. These samples were evaluated on a Bruker Kappa goniometer coupled with a Bruker APEX II Ultra diffractometer using Mo Kα (λ = 0.7093 Å) radiation at 40 kV and 40 mA within a Debye–Scherrer geometry.

X-ray photoelectron spectroscopy (XPS) data was gathered using the AXIS Supra XPS from Kratos Analytical. The S 2p, P 2p, C 1s, and F 1s spectra were compiled and analyzed using CasaXPS software.

Focused ion beam (FIB-SEM) was used to characterize the surface and cross-section morphology of the NPS films. The exposed and heat-treated films were mounted onto an SEM sample stage (Ted Pella) and transferred into the FEI Scios DualBeam FIB-SEM using the air-sensitive holder to avoid ambient air exposure. The exposed samples were prepared in a glovebox and sealed before being transferred to the focused ion beam scanning electron microscopy (FIB-SEM) instrument, effectively preventing contamination. EDS mapping was collected using a 10 kV electron beam with a current of 0.1 nA.

Raman spectroscopy was performed using a Renishaw inVia Raman Microscope and a 532 nm laser source. Due to the samples' air sensitivity, all samples were sealed in two thin glass slides in the glove box and directly exposed to the laser beam during testing.

TEM images were captured using Titan Cubed Themis Z 60–300, Thermo Fisher Scientific, with aberration correction, an X-FEG source, and a Bruker Super-X EDX detector. The test was operated at 300 kV, with a 30 pA beam current, a 21.5 mrad convergence semi-angle, and an 80–379 mrad collection semi-angle. Atomistic models were generated using Crystalmaker software and Fast Fourier transform (FFT) patterns. The inverse analyses and radial intensity profiles were conducted using DigitalMicrograph (Gatan) software.

Electrochemical Characterization: The ionic conductivity of the pre-Na agent was measured by the DC polarization method using a symmetrical cell (Na_9Sn_4 || NPS || pre-Na agent || NPS || Na_9Sn_4). All materials were added in a 10 mm Polyetheretherketone (PEEK) die and pressed at 70 MPa with titanium plungers. The NPS layers between the Na-Sn alloy, performing as the sodium source, and the pre-Na agent serve as the electron block

layer to avoid short circuits from carbon. The σ_{Na+} of the pre-Na agent with different Na_2S-NPS ratios was determined from the obtained value after applying a 0.1 V bias voltage for 300s, using Bio-Logic VSP-300.

Electrochemical impedance spectroscopy (EIS) was measured with a frequency range from 7 MHz to 1 Hz and an AC amplitude of 10 mV using Bio-Logic VSP-300. To test the EIS revolution of the pre-Na agent, the cell configuration as pre-Na || NPS || Na_9Sn_4 was assembled and charged at 0.1C for 10h. To avoid the reaction between the NPS and Na_9Sn_4 anode, which complicates the analysis and makes it challenging to identify the reaction on the cathode side, NBH was added between the SE layer and anode as an isolation layer. A 6 mg pre-Na agent was weighed and placed on the NPS-NBH electrolyte layer as the cathode.

DC polarization was collected by directly testing the pre-Na agent between the Ti plungers, while a potential bias of 1 V was exerted to stimulate the electrochemical reaction.

Solid-state batteries were assembled in a 10 mm PEEK die with two Ti plungers. For pellet cell assembly, 100 mg of commercial halide solid electrolyte (99.9%, Unigrid, USA) was pressed under 110 MPa to form a rigid pellet without cracks as the support layer with a thickness of ≈400 µm. To relieve the interfacial reaction at the SE-anode interface, 10 mg NCBH (99.9%, Unigrid, USA) was added to form an isolated layer. For the presodiated cells, a 3% or 5% mass ratio of the pre-Na agent was mixed with NCO or NFM cathode composites. The NCO cathode composite was manually prepared by mixing $NaCrO_2$ active materials, halide SE, and vapor-grown carbon fibers (VGCF) in a 50:48:2 weight ratio and added to one side of the SE pellet. Since the NFM cathode has a lower conductivity than NCO, an extra ball milling step was required to help improve the cell performance. 0.4 g tin or antimony powder was weighed and mixed with 0.2 g CNT for anodes. Then, the mixture was distributed in 0.3 g DI water in a THINKY Mixer at 1800 rpm for 20 min.

The configuration of full cells was shown as NCO/NFM || halide SE || Sn/Sb. The assembled cells with all three parts were pressed again at 270 MPa before electrochemical testing. The cells were cycled using a Neware Battery cycler at room temperature and under pressure at ≈75 MPa.

Supporting Information

Supporting Information is available from the Wiley Online Library or from the author.

Acknowledgements

The National Science Foundation funded this work through the Future Manufacturing (FM) grant No. 2134764. This work was partly performed at the San Diego Nanotechnology Infrastructure (SDNI) of UCSD, a National Nanotechnology Coordinated Infrastructure member, supported by the National Science Foundation (grant ECCS-2025752). The authors acknowledge using facilities and instrumentation at the UC Irvine Materials Research Institute (IMRI), partly supported by the National Science Foundation through the UC Irvine Materials Research Science and Engineering Center (DMR-2011967). Specifically, the XPS work was performed using instrumentation funded in part by the National Science Foundation Major Research Instrumentation Program under grant no. CHE-1338173.

Conflict of Interest

A Patent disclosure related to this work has been filed through UCSD's OIC.

Author Contributions

W.T. and D.X. contributed equally to this work. W.T. and D.X. conceived the concept and designed the cell architecture. D.X. conducted the electrochemical measurements and analyzed all material characterization data. XRD and TEM were done by D.X. D.L. captured FIB-SEM images. J.W. carried out the XPS and collected SEM images. A.F. collected the Raman data. D.X. initially drafted and revised the manuscript with W.T. W.B. and F.L. contributed to the scientific discussions. All authors approved the final version of the manuscript. Z.C. directed the project and provided critical guidance and instructions throughout the work.

Data Availability Statement

The data that support the findings of this study are available from the corresponding author upon reasonable request.

Keywords

energy density, mixed electron-ion network, presodiation strategy, sodium all-solid-state batteries, sodium sulfide

Received: December 2, 2024
Revised: January 21, 2025
Published online:

[1] C. Zhao, L. Liu, X. Qi, Y. Lu, F. Wu, J. Zhao, Y. Yu, Y. Hu, L. Chen, *Adv. Energy Mater.* **2018**, *8*, 1703012.
[2] L. Ran, M. Li, E. Cooper, B. Luo, I. Gentle, L. Wang, R. Knibbe, *Energy Storage Mater.* **2021**, *41*, 8.
[3] J. Yang, G. Liu, M. Avdeev, H. Wan, F. Han, L. Shen, Z. Zou, S. Shi, Y.-S. Hu, C. Wang, X. Yao, *ACS Energy Lett.* **2020**, *5*, 2835.
[4] H. Gao, L. Xue, S. Xin, K. Park, J. B. Goodenough, *Angew. Chem.* **2017**, *129*, 5633.
[5] L. Xiao, H. Lu, Y. Fang, M. L. Sushko, Y. Cao, X. Ai, H. Yang, J. Liu, *Adv. Energy Mater.* **2018**, *8*, 1703238.
[6] Z. Li, Y. Chen, Z. Jian, H. Jiang, J. J. Razink, W. F. Stickle, J. C. Neuefeind, X. Ji, *Chem. Mater.* **2018**, *30*, 4536.
[7] C. Chi, Z. Liu, X. Lu, Y. Meng, C. Huangfu, Y. Yan, Z. Qiu, B. Qi, G. Wang, H. Pang, T. Wei, Z. Fan, *Energy Storage Mater.* **2023**, *54*, 668.
[8] X. Wang, C. Zhang, M. Sawczyk, J. Sun, Q. Yuan, F. Chen, T. C. Mendes, P. C. Howlett, C. Fu, Y. Wang, X. Tan, D. J. Searles, P. Král, C. J. Hawker, A. K. Whittaker, M. Forsyth, *Nat. Mater.* **2022**, *21*, 1057.
[9] X. Chi, F. Hao, J. Zhang, X. Wu, Y. Zhang, S. Gheytani, Z. Wen, Y. Yao, *Nano Energy* **2019**, *62*, 718.
[10] E. Matios, H. Wang, C. Wang, X. Hu, X. Lu, J. Luo, W. Li, *ACS Appl. Mater. Interfaces* **2019**, *11*, 5064.
[11] Y. Zhu, Q. Yao, R. Shao, C. Wang, W. Yan, J. Ma, D. Liu, J. Yang, Y. Qian, *Nano Lett.* **2022**, *22*, 7976.
[12] L. Liu, F. Xie, J. Lyu, T. Zhao, T. Li, B. G. Choi, *J. Power Sources* **2016**, *321*, 11.
[13] J. A. Lewis, K. A. Cavallaro, Y. Liu, M. T. McDowell, *Joule* **2022**, *6*, 1418.
[14] S. Y. Han, C. Lee, J. A. Lewis, D. Yeh, Y. Liu, H.-W. Lee, M. T. McDowell, *Joule* **2021**, *5*, 2450.
[15] X. Liu, Y. Tan, T. Liu, W. Wang, C. Li, J. Lu, Y. Sun, *Adv. Funct. Mater.* **2019**, *29*, 50.
[16] F. Ding, Q. Meng, P. Yu, H. Wang, Y. Niu, Y. Li, Y. Yang, X. Rong, X. Liu, Y. Lu, L. Chen, Y. Hu, *Adv. Funct. Mater.* **2021**, *31*, 2101475.
[17] M. Liu, J. Zhang, S. Guo, B. Wang, Y. Shen, X. Ai, H. Yang, J. Qian, *ACS Appl. Mater. Interfaces* **2020**, *12*, 17620.
[18] J. A. S. Oh, G. Deysher, P. Ridley, Y. Chen, D. Cheng, A. Cronk, S. Ham, D. H. S. Tan, J. Jang, L. H. B. Nguyen, Y. S. Meng, *Adv. Energy Mater.* **2023**, *13*, 26.
[19] Y. Xu, H. Sun, C. Ma, J. Gai, Y. Wan, W. Chen, *Chin. J. Chem. Eng.* **2021**, *39*, 261.
[20] H. Wang, Y. Xiao, C. Sun, C. Lai, X. Ai, *RSC Adv.* **2015**, *5*, 106519.

[21] F. Li, X. Yu, K. Tang, X. Peng, Q. Zhao, B. Li, *J. Appl. Electrochem.* **2023**, *53*, 9.
[22] J. H. Jo, J. U. Choi, Y. J. Park, J. K. Ko, H. Yashiro, S.-T. Myung, *Energy Storage Mater.* **2020**, *32*, 281.
[23] S. Mirza, Z. Song, H. Zhang, A. Hussain, H. Zhang, X. Li, *J. Mater. Chem. A* **2020**, *8*, 23368.
[24] K. Fang, Y. Tang, J. Liu, Z. Sun, X. Wang, L. Chen, X. Wu, Q. Zhang, L. Zhang, Y. Qiao, S.-G. Sun, *Nano Lett.* **2023**, *23*, 6681.
[25] D. Dewar, A. M. Glushenkov, *Energy Environ. Sci.* **2021**, *14*, 1380.
[26] Y. Cao, G. Li, J. Chen, J. Xu, X.-L. Li, N. Wang, X. Zhang, M. Liao, Y. Liu, X. Dong, Y. Wang, Y. Xia, *J. Power Sources* **2023**, *587*, 233718.
[27] J. M. Stratford, M. Mayo, P. K. Allan, O. Pecher, O. J. Borkiewicz, K. M. Wiaderek, K. W. Chapman, C. J. Pickard, A. J. Morris, C. P. Grey, *J. Am. Chem. Soc.* **2017**, *139*, 7273.
[28] J.-M. Liang, L.-J. Zhang, D.-G. XiLi, J. Kang, *Rare Met.* **2020**, *39*, 1005.
[29] V. Kumar, A. Y. S. Eng, Y. Wang, D.-T. Nguyen, M.-F. Ng, Z. W. Seh, *Energy Storage Mater.* **2020**, *29*, 1.
[30] Y. Chen, Y. Zhu, Z. Sun, X. Kuai, J. Chen, B. Zhang, J. Yin, H. Luo, Y. Tang, G. Zeng, K. Zhang, L. Li, J. Xu, W. Yin, Y. Qiu, Y. Zou, Z. Ning, C. Ouyang, Q. Zhang, Y. Qiao, S. Sun, *Adv. Mater.* **2024**, *36*, 2407720.
[31] J. Qian, Y. Xiong, Y. Cao, X. Ai, H. Yang, *Nano Lett.* **2014**, *14*, 1865.
[32] S. Hua, G. Cao, Y. Cui, *J. Power Sources* **1998**, *76*, 112.
[33] K. Raz, P. Tereshchuk, D. Golodnitsky, A. Natan, *J. Phys. Chem. C* **2018**, *122*, 16473.
[34] J. M. D. Ilarduya, L. Otaegui, M. Galcerán, L. Acebo, D. Shanmukaraj, T. Rojo, M. Armand, *Electrochim. Acta* **2019**, *321*, 134693.
[35] M. Sathiya, J. Thomas, D. Batuk, V. Pimenta, R. Gopalan, J.-M. Tarascon, *Chem. Mater.* **2017**, *29*, 5948.
[36] J. H. Jo, J. U. Choi, Y. J. Park, J. Zhu, H. Yashiro, S.-T. Myung, *ACS Appl. Mater. Interfaces* **2019**, *11*, 5957.
[37] X. Li, W. Li, J. Yu, H. Zhang, Z. Shi, Z. Guo, *J. Alloy. Compd.* **2017**, *724*, 932.
[38] J.-H. Choi, C.-W. Ha, H.-Y. Choi, H.-C. Shin, C.-M. Park, Y.-N. Jo, S.-M. Lee, *Electrochim. Acta.* **2016**, *210*, 588.
[39] A. Y. S. Eng, V. Kumar, Y. Zhang, J. Luo, W. Wang, Y. Sun, W. Li, Z. W. Seh, *Adv. Energy Mater.* **2021**, *11*, 14.
[40] H. Nakajima, H. Tsukasaki, J. Ding, T. Kimura, T. Nakano, A. Nasu, A. Hirata, A. Sakuda, A. Hayashi, S. Mori, *J. Power Sources* **2021**, *511*, 230444.
[41] T. Famprikis, O. U. Kudu, J. A. Dawson, P. Canepa, F. Fauth, E. Suard, M. Zbiri, D. Dambournet, O. J. Borkiewicz, H. Bouyanfif, S. P. Emge, S. Cretu, J.-N. Chotard, C. P. Grey, W. G. Zeier, M. S. Islam, C. Masquelier, *J. Am. Chem. Soc.* **2020**, *142*, 18422.
[42] D. Xu, W. Tang, F. Li, K. Zhou, J. Wu, A. Fuqua, Y. Chen, D. J. Lee, J. Qin, A. R. Tao, P. Liu, Z. Chen, *ACS Energy Lett.* **2024**, *9*, 2293.
[43] Y. Tian, T. Shi, W. D. Richards, J. Li, J. C. Kim, S.-H. Bo, G. Ceder, *Energy Environ. Sci.* **2017**, *10*, 1150.
[44] X. Wang, B. He, B. Liu, M. Avdeev, S. Shi, *Adv. Funct. Mater.* **2024**, *34*, 44.
[45] M. Hofer, M. Grube, C. F. Burmeister, P. Michalowski, S. Zellmer, A. Kwade, *Adv. Powder Technol.* **2023**, *34*, 104004.
[46] L. Lin, C. Zhang, Y. Huang, Y. Zhuang, M. Fan, J. Lin, L. Wang, Q. Xie, D. Peng, *Small* **2022**, *18*, 2107368.
[47] J. Li, D. Liu, H. Sun, D. Qu, Z. Xie, H. Tang, J. Liu, *SmartMat.* **2023**, *4*, e1200.
[48] N. Tanibata, M. Deguchi, A. Hayashi, M. Tatsumisago, *Chem. Mater.* **2017**, *29*, 5232.
[49] S. Wenzel, T. Leichtweiss, D. A. Weber, J. Sann, W. G. Zeier, J. Janek, *ACS Appl. Mater. Interfaces* **2016**, *8*, 28216.
[50] Y. Zhao, J. Liang, Q. Sun, L. V. Goncharova, J. Wang, C. Wang, K. R. Adair, X. Li, F. Zhao, Y. Sun, R. Li, X. Sun, *J. Mater. Chem. A* **2019**, *7*, 4119.
[51] L. Fan, R. Ma, Y. Yang, S. Chen, B. Lu, *Nano Energy* **2016**, *28*, 304.
[52] N. Wang, Y. Wang, Z. Bai, Z. Fang, X. Zhang, Z. Xu, Y. Ding, X. Xu, Y. Du, S. Dou, G. Yu, *Energy Environ. Sci.* **2019**, *13*, 562.
[53] S. Wei, S. Xu, A. Agrawral, S. Choudhury, Y. Lu, Z. Tu, L. Ma, L. A. Archer, *Nat. Commun.* **2016**, *7*, 11722.
[54] A. Nasu, T. Inaoka, F. Tsuji, K. Motohashi, A. Sakuda, M. Tatsumisago, A. Hayashi, *ACS Appl. Mater. Interfaces* **2022**, *14*, 24480.
[55] J. Zhou, Y. Yang, Y. Zhang, S. Duan, X. Zhou, W. Sun, S. Xu, *Angew. Chem., Int. Ed.* **2021**, *60*, 10129.
[56] D. H. S. Tan, E. A. Wu, H. Nguyen, Z. Chen, M. A. T. Marple, J.-M. Doux, X. Wang, H. Yang, A. Banerjee, Y. S. Meng, *ACS Energy Lett.* **2019**, *4*, 2418.
[57] Y. Lu, C.-Z. Zhao, J.-Q. Huang, Q. Zhang, *Joule* **2022**, *6*, 1172.
[58] J. P. Schmidt, T. Chrobak, M. Ender, J. Illig, D. Klotz, E. Ivers-Tiffée, *J. Power Sources* **2011**, *196*, 5342.